Reconfigurable Multimode Millimeter-Wave Three-State Phased Antenna Array

Zhonghe Zhang, *Member, IEEE*, Sai-Wai Wong, *Senior Member, IEEE*, Jing-Yu Lin, *Member, IEEE*,
Jiupei Shi, Wenting Li, *Member, IEEE*, Long Zhang, *Member, IEEE*,
Chaoyun Song, *Senior Member, IEEE*, and Yejun He, *Senior Member, IEEE*

Abstract—Traditional phased array needs to use multiple arrays with multiple ports to cover different direction. This article introduces a single radiation element to achieve beam scanning by combining mechanically reconfigurable antennas with phased arrays. By using metallic coverage walls to control the TE_{101} and TM_{110} modes within the metal cavity, multidirectional three-state radiation is achieved, such as endfire, oblique, and broadside. Combined with phased arrays, this approach enables multidirectional beam scanning by using single radiation elements instead of using traditional multiple arrays. Finally, a 1×4 mm-wave cavity antenna array is fabricated and measured to verify its beam scanning and three-state directional reconfigurability. The measured prototype achieves a $50°$ beam coverage and high gain in three directions, validating the proposed concept. This concept can be applied to millimeter-wave 5G or 6G future communications, expanding the antenna beam-scanning range.

Index Terms—Millimeter wave, multimode cavity, phased array, radiation-pattern reconfigurable antenna, three state.

I. INTRODUCTION

RECONFIGURABLE antennas are gaining significant attention [1], [2], [3], [4], [5], [6], [7], [8], [9], [10], [11], [12] due to their ability to improve system efficiency, boost communication quality, and meet the diverse requirements of various scenarios. To achieve extensive spatial coverage

and ensure consistent communication quality, the potential of reconfigurable antenna technology is being actively explored in emerging wireless communication systems, such as 5G and 6G. The effective method of using electronically controlled components for antenna reconfiguration includes frequency [9], [10] and polarization [14], [15] reconfiguration. Importantly, extensive research has been conducted on pattern reconfiguration [16], [17], [18], showcasing its importance. In [17], the integration of four p-i-n diodes achieved the reconfigurability of the antenna's radiation pattern. In [18], a p-i-n diode-controlled radiation pattern reconfigurable phased array is proposed. It significantly reduces the array count and transmitter-receiver components while maintaining identical spatial coverage.

However, these electronically driven reconfigurable antennas often encounter the issues of high loss, high noise, low power capability, and complex integration due to installation of electronic components. Due to the limitation of electronically driven phased antenna array, most of the practical commercial applications use the combination of mechanical and electronic reconfiguration antenna array, such as Starlink ground base unit [37]. In order to overcome these disadvantages, mechanically reconfigurable antennas have been proposed. In the microwave frequency range, using fluid structures is an effective method for achieving mechanically reconfigurable antennas [19], [20], [21]. In [19], liquid metal is employed to manipulate the antenna's beam direction and beamwidth. In [21], a study focused on using liquid flow to modify the existence of parasitic dielectric resonator antennas, creating different radiation patterns and polarization. In [22], a method is introduced that involves tuning movable metallic pillars inside metallic cavity-backed slot antennas to achieve frequency reconfigurability. Similarly, this method can tune both the polarization and frequency of the array [23]. Through the use of a piezoelectric tuning disk, Semnani et al. [24] change the critical gap size of the resonator to achieve frequency adjustability. Mechanical rotation [25] and variable focusing [26] are also effective methods for reconfiguring antenna beams.

5G, 6G base stations, and satellite communications impose higher standards on reconfigurable antenna arrays in the millimeter-wave range. Size constraints, machining precision issues, and the need for additional control circuits and complex mechanical systems lead to ongoing challenges in achieving reconfigurability for millimeter-wave antennas. In [27], the

method of utilizing polarization standing waves (PSWs) to achieve frequency reconfigurability in Fabry–Pérot cavities (FPCs) antennas is employed. In [28], reconfigurable antennas capable of multiple linear polarizations (LPs) in the millimeter-wave frequency band were designed. The antennas utilized an inflatable cavity resonating in the TM_{510} mode as their base. Five different reconfigurable states can be achieved through mechanical rotation. In [29], graphene resistance tuning enabled directional reconfigurability for millimeter wave in Vivaldi antennas.

Current antenna designs aiming for wide spatial beam coverage in both endfire and broadside configurations often necessitate complex integration using multiple arrays for various directions [30], [31]. The concept of multimode antennas was introduced in [32] and [33], where multiple ports became an effective means to achieve multimode characteristics. In [34], the orthogonal electromagnetic properties of different modes were utilized to achieve the independent excitation of multiple modes. Currently, no literature has proposed a reconfiguration method using metal cover wall. This article utilizes metal cover walls to achieve radiation control of cavity antennas, enabling widebeam coverage from endfire to broadside, which can be applied to communication needs in millimeter-wave base stations, high-orbit satellites, relay satellites, and space stations. Overall, exploring new and stable reconfiguration methods for millimeter-wave beamforming is a meaningful research direction.

This article proposed a millimeter-wave phased array based on metal cover wall to select radiation states within metal cavities. By combining mechanical reconfigurability with phased arrays, it achieves an extensive spatial coverage for millimeter wave in terms of broadside, oblique, and endfire radiation. The contribution of this article is described as follows.

1) A new tuning method is introduced in the literature, which employs metal cover wall to enable beamforming reconfigurability in full-metal cavity antennas.
2) Traditionally, the reconfigurable antennas are focused on antenna unit-level reconfigurability, whereas the proposed metal cover wall approach is suitable for antenna array-level reconfigurability. This reconfiguration method demonstrates good feasibility in the millimeter-wave domain, providing a viable solution for beam reconfigurability in high-power millimeter-wave or terahertz antennas, suitable for future 5G or 6G communication systems.
3) Compared to multipanel arrays, this article achieves beam coverage in multiple directions in the form of a linear array and implements phased scanning in the endfire, oblique, and broadside directions. The metal cover wall approach provides a solution for enhancing wide spatial beam-scanning coverage in millimeter-wave systems.

II. ANTENNA DESIGN

A. Principle of Cavity Resonator

Fig. 1(a) depicts the model of a multimode resonator within a single rectangular cavity, with the cavity being square-shaped
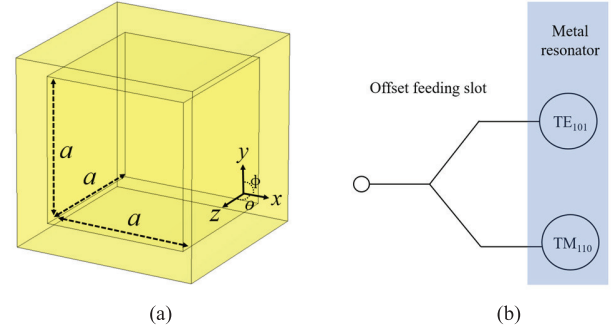

Fig. 1. (a) Model of the multimode resonator in a single rectangular cavity. (b) Cavity mode topology.

and having dimensions of a for length, width, and height. The resonance frequency is derived from the following equation:

$$f_{mnl} = \frac{\upsilon}{2\pi \sqrt{\mu_r \varepsilon_r}} \sqrt{\left[\left(\frac{m\pi}{a}\right)^2 + \left(\frac{n\pi}{a}\right)^2 + \left(\frac{l\pi}{a}\right)^2\right]}$$
$$= \frac{\upsilon \sqrt{(m^2 + n^2 + l^2)}}{2a \sqrt{\mu_r \varepsilon_r}}. \tag{1}$$

Within the equation, f_{mnl} signifies the resonance frequency, while m, n, and l are the resonance mode numbers, and μ_r and ε_r represent the magnetic permeability and permittivity of vacuum, respectively [35]. The speed of light is represented by υ. When accounting for the fundamental modes TE_{101} and TM_{110}, the resonance frequency is expressed as

$$f_{101} = \frac{\sqrt{2}\upsilon}{2a \sqrt{\mu_r \varepsilon_r}} \tag{2}$$

$$f_{110} = \frac{\sqrt{2}\upsilon}{2a \sqrt{\mu_r \varepsilon_r}}. \tag{3}$$

From (2) to (3), it is evident that the resonance frequencies of both fundamental modes are identical. Fig. 1(b) illustrates the cavity mode topology. The offset feeding slot simultaneously excites the two fundamental modes, e.g., TE_{101} and TM_{110}. Fig. 2 shows the electromagnetic field distribution of these two excited fundamental modes of the cavity resonator. In Fig. 2(a), it showcases the electromagnetic field distribution of the TE_{101} mode, while Fig. 2(b) displays the electromagnetic field distribution of the TM_{110} mode. TE_{101} mode's electric field is parallel to the y-axis, while the TM_{110} mode's electric field is parallel to the z-axis. The electric field directions of these two different modes are perpendicular to each other, enabling radiation in different directions.

Fig. 3 illustrates the designed cavity antenna, with Fig. 3(a) showcasing the antenna's 3-D view. The antenna structure consists of a metal cavity, with air inside and metal walls on the outside. Inside is a cavity with dimensions a_1 for length, width, and height, designed with a chamfer radius of r to accommodate millimeter-wave computer numerical control (CNC) fabrication. Radiating slot 1 is shown in the front view, while radiating slot 2 is displayed in the top view, and the back view illustrates the feeding slot offset from the center. It is a full-metal antenna structure that uses slots for feeding and radiation.
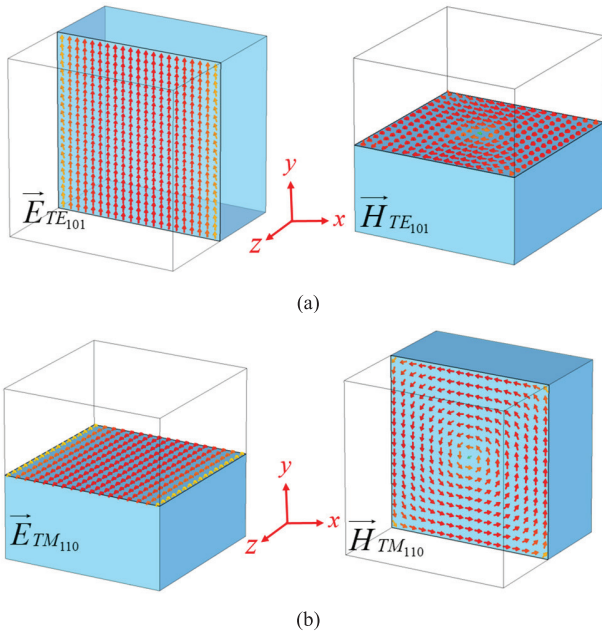
Fig. 2. Electromagnetic field distribution of a cavity resonator. (a) TE_{101}. (b) TM_{110}.

Fig. 4. H-field distributions of the triple modes. (a) TE_{101}. (b) TM_{110}. (c) $TE_{101} + TM_{110}$.

with a metal cover wall while leaving the slot in the $+y$-direction uncovered, the magnetic field becomes parallel to the long edge of the radiating slot in State 2, thereby enabling antenna radiation in the $+y$-direction. Fig. 4(c) is State 3, no metal cover walls are present, and both modes are excited simultaneously. This indicates the simultaneous operation of antenna radiating slots 1 and 2, allowing the radiation direction to be determined using Poynting's theorem

$$\overrightarrow{P_t} = \nabla \cdot (\overrightarrow{E_t} \times \overrightarrow{H_t}) \tag{4}$$

$$\overrightarrow{E_t} = \overrightarrow{E_1} + \overrightarrow{E_2} \tag{5}$$

$$\overrightarrow{H_t} = \overrightarrow{H_1} + \overrightarrow{H_2}. \tag{6}$$

In this context, $\overrightarrow{P_t}$ stands for the Poynting electromagnetic vector, with the electric field vector labeled as $\overrightarrow{E_t}$ and the magnetic field vector as $\overrightarrow{H_t}$. The Poynting vector is perpendicular to both the $\overrightarrow{E_t}$ vector and $\overrightarrow{H_t}$ vector. Solving for the direction of the $\overrightarrow{E_t}$ vector allows determination of the radiation direction of the cavity antenna. Fig. 4(c) indicates that the electric field orientations of radiating slots 1 and 2 are mutually perpendicular, whereas the magnetic fields of slots 1 and 2 are parallel.

According to (5) and (6), the addition of electromagnetic field vectors from both slots results in beam merging in both endfire and broadside directions, achieving oblique radiation direction.

The topology of three radiation modes is depicted in Fig. 5. The metal cover wall acts like a switch, tuning the beam range of the antenna on its outer surface. State 1 represents a broadside radiation mode, where the metal cover wall on the $+y$ plane obstructs radiating slot 2, exciting the TE_{101} mode
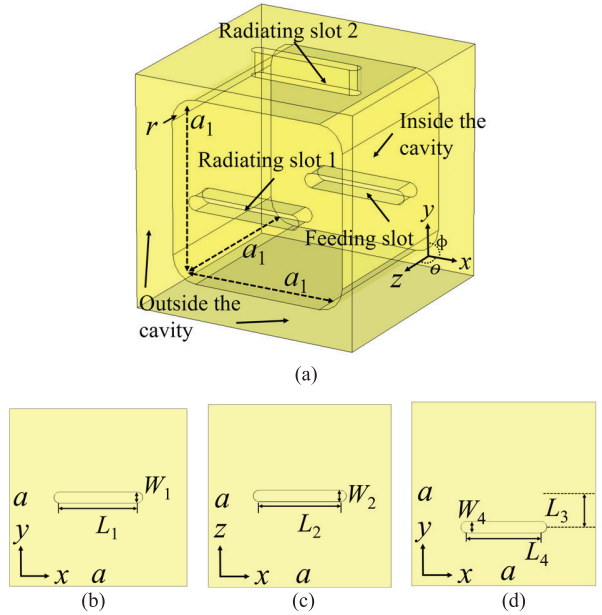

Fig. 3. Proposed cavity antenna. (a) 3-D view. (b) Front view. (c) Top view. (d) Back view.

The antenna utilizes metal cover walls to control three different radiation states. In Fig. 4, H-field distributions for the triple states are depicted. Fig. 4(a) represents the excited TE_{101} mode, where red arrows indicate its magnetic field aligned with radiating slot 1. By covering the slot in the $+y$-direction with a metal cover wall while leaving the slot in the $+z$-direction uncovered, the magnetic field becomes parallel to the long edge of the radiating slot in State 1, thereby enabling antenna radiation in the $+z$-direction. In Fig. 4(b), the excited TM_{110} mode shows the magnetic field parallel to radiating slot 2. By covering the slot in the $+z$-direction
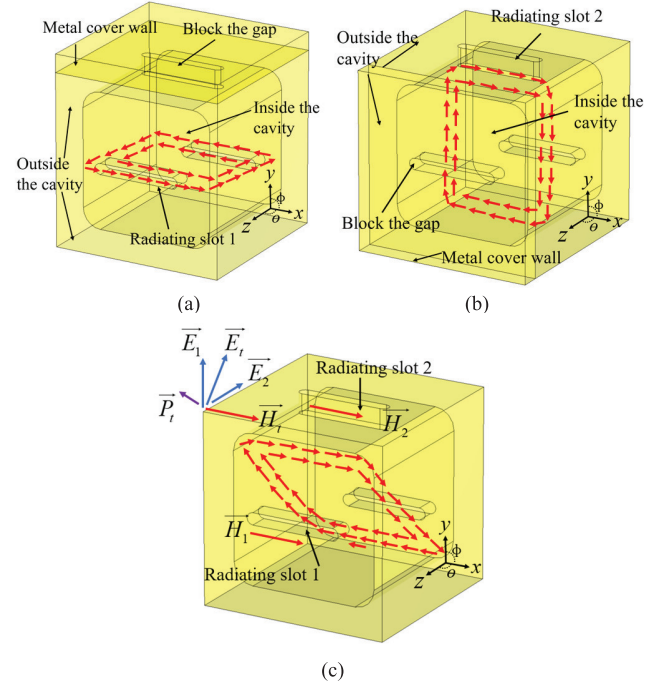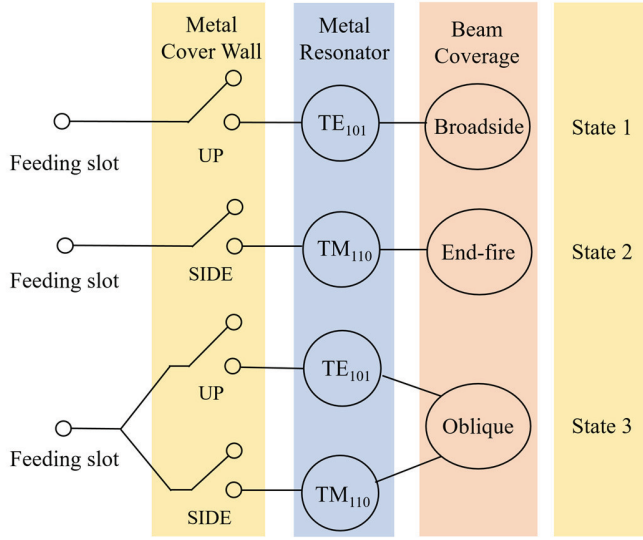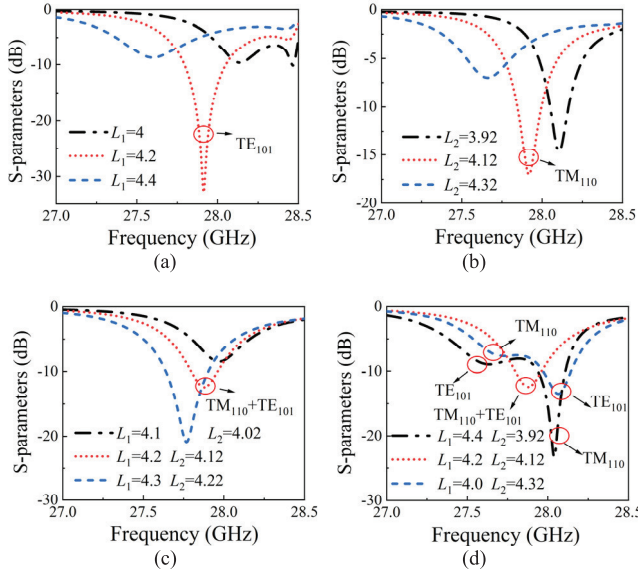
Fig. 5. Topology of three radiation modes.

Fig. 6. Effect of the sizes of the radiating slots on the cavity modes. (a) L_1. (b) L_2. (c) and (d) L_1 and L_2. Dimensional unit: mm.
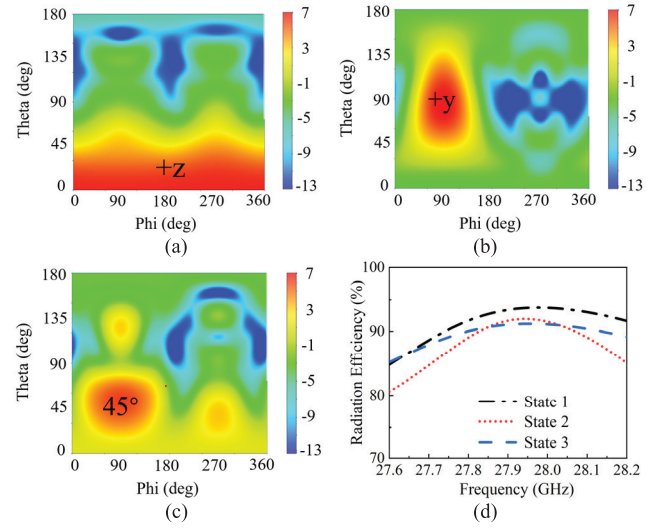

Fig. 7. Contour plot depicting the simulated 3-D radiation pattern of the antenna and radiation efficiency. (a) Broadside. (b) Endfire. (c) Oblique. (d) Radiation efficiency.

inside the cavity. This results in vertically polarized waves in the $+z$-direction from radiating slot 1. In the broadside radiation state, represented by State 2, the metal cover wall on the $+z$ plane blocks radiating slot 1. During this state, the cavity operates in TM_{110} mode, generating vertically polarized waves in the $+y$-direction from radiating slot 2. In the oblique radiation state, denoted as State 3, no metal cover wall is present. Within the cavity, both TE_{101} and TM_{110} modes are concurrently active. Radiating slots 1 and 2 work simultaneously, creating an oblique beam. Although all three states are vertically polarized, the radiation directions of the three states are not consistent.

The effect of the sizes of the radiating slots on the cavity modes is shown in Fig. 6. In Fig. 6(a), representing State 1, altering the length L_1 of radiating slot 1 adjusts the TE_{011} mode. When L_1 increases, the resonant frequency shifts toward

lower frequencies, while decreasing L_1 shifts it toward higher frequencies. In Fig. 6(b), showing State 2, changing the length L_2 of radiating slot 2 tunes the cavity's TM_{110} mode. An increase in L_2 causes a shift toward lower resonant frequencies, while a decrease shifts it toward higher frequencies. In Fig. 6(c), representing State 3, when both L_1 and L_2 increase, the resonant frequency shifts toward lower frequencies; conversely, it shifts toward higher frequencies when they decrease. Fig. 6(d) represents state 3. When L_1 increases and L_2 decreases, it tunes the two modes to higher and lower frequencies, respectively. Conversely, when L_1 decreases and L_2 increases, it tunes the two modes to lower and higher frequencies, respectively. The cavity modes are independently controlled by exciting them through various metal cover walls.

The simulated contour plot of the 3-D radiation pattern of the antenna, as shown in Fig. 7(a)–(c), indicates that the antenna's radiation spans a range covering beams from the broadside, oblique, and endfire directions. The radiation efficiency for the three states is shown in Fig. 7(d). The radiation efficiency for the three states is 93.39%, 91.75%, and 91.09%, respectively, all maintaining good radiation performance.

B. Antenna Array Design

For the purpose of achieving substantial gain and extensive beam coverage, a 1×4 phased array antenna is evenly arranged along the x-axis. The antenna is composed of two structures. The cavity antenna, constructed from metallic material, utilizes a single-layer dielectric substrate and two layers of metal specifically designed to enable antenna feeding and connection with the phased array module.

The substrate is Rogers 5880 with a thickness of 0.787 mm. Refer to Fig. 8 for the geometrical configuration of the feeding circuit. The yellow area represents the metal covering layer, while the red area signifies the metal via holes. r_2 refers to ordinary through-holes utilized for securing the substrate and antenna structure through screw fastening. The substrate's rear
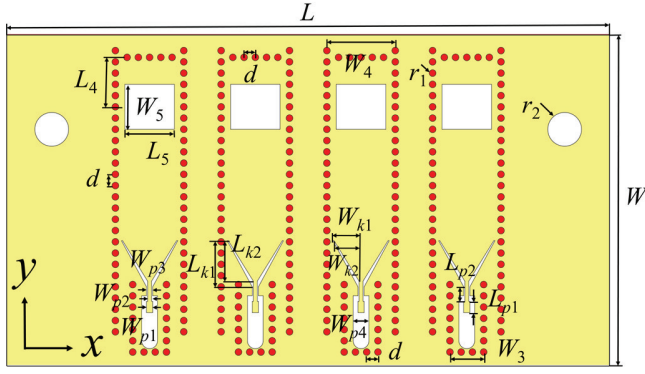
Fig. 8. Geometrical configuration of the feeding circuit.

TABLE I
PARAMETERS RELATING TO ANTENNA IN FIGS. 4 AND 7 (UNIT: MM)

a	9.4	L_1	4.2	W_1	0.6	W_{p1}	0.55
a_1	7.4	L_2	4.12	W_2	0.6	W_{p2}	0.35
d	1	L_3	3.8	W_3	0.6	W_{p3}	0.55
r_1	0.6	L_4	4.4	W_4	6.08	W_{p4}	1.4
r_2	1.5	L_5	4.4	W_5	4	L	53.6
L_{p1}	1	L_{k1}	4.1	W_{k1}	2.3	W	29.4
L_{p2}	1.3	L_{k2}	3.6	W_{k2}	2.2	r	1

Fig. 9. Geometrical configuration of the phased antenna array.

Fig. 10. Contour plot depicting the simulated 3-D radiation pattern of the phased antenna array. (a) Broadside. (b) Endfire. (c) Oblique.

itself has a wide beamwidth. In addition, the design considers the impact of the Mini-SMP interface on antenna radiation, leading to a significant increase in sidelobes. However, this issue can be avoided in practical system implementations with on-board feeding, which eliminates the need for transition to VNA connection.

III. MEASUREMENT AND ANALYSIS

A. State 1

Utilizing CNC technology, the antenna is processed, showcasing the experimental setup of State 1 in the phased antenna array, as depicted in Fig. 11. In Fig. 11(a), the simulated antenna structure displays a metal cover wall obstructing the cavity gap in the +y-direction. By adjusting the phase difference between ports 1 and 4, it facilitates beam scanning in the broadside direction. Fig. 11(b) displays the fabricated antenna structure, while Fig. 11(c) illustrates the testing environment. The Beamform Box (BBOX) [36] can provide varying beam amplitudes and different phases for each antenna port, interconnecting with the antenna via four RF coaxial cables. During practical testing, absorptive materials will be employed to shield the BBOX and minimize beam scattering.

As shown in Fig. 12(a), both simulated and measured reflection coefficients at symmetric ports, namely, ports 1 and 2,
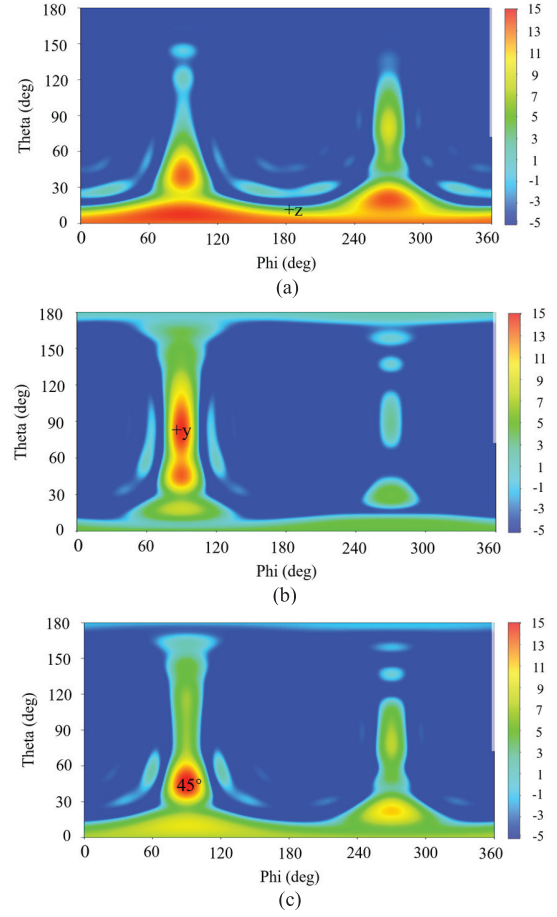
side features a metal covering. Dimensions for the feeding circuit are listed in Table I.

Fig. 9 depicts the geometrical configuration of the phased antenna array. There exist four radiation slot antenna elements along both the +z- and +y-directions. Furthermore, the +z- and +y-directions feature metal cover wall faces, yet these are not visually represented in the diagram. Mini Subminiature Push-On (Mini-SMP) connectors serve as the feeding line for connecting to vector network analyzer (VNA), transitioning subsequently into substrate-integrated waveguide (SIW) to feed the metallic cavity antenna from its backside. The four ports are sequentially labeled as port 1 to port 4.

The contour plot in Fig. 10 demonstrates the simulated 3-D radiation pattern of the phased antenna array. A noticeable enhancement in antenna gain and a narrower radiation beam are observed compared to Fig. 7. In Fig. 10(a), the antenna
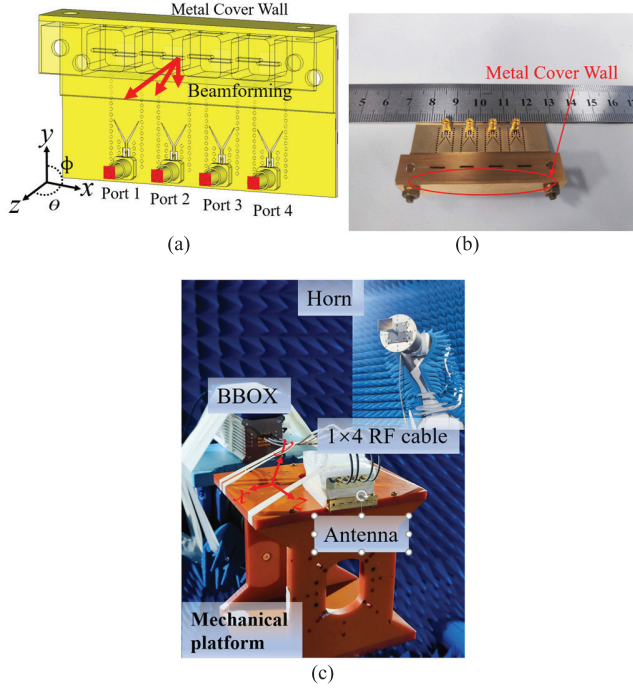
(a)

(b)

(c)

Fig. 11. State 1 geometrical configuration of the phased antenna array. (a) Simulation. (b) Fabrication. (c) Experimental setup.

(b)

(b)

Fig. 12. State 1. (a) Simulated and measured reflection coefficients for ports 1 and 2. (b) Simulated and measured between nearby ports (solid: simulation and dashed: measurement).

indicate return losses below -10 dB at 27.91 GHz. As shown in Fig. 12(b), the simulated and measured return losses between adjacent ports are both below -20 dB at 27.91 GHz, demonstrating strong isolation between the neighboring ports.

The simulated and measured results within the band are reasonably match with each other. The ripple observed is attributed to errors in the test cables and hand soldering during measurements, which is hard to calibrate.

Fig. 13 depicts the simulated and measured element radiation patterns. When a single port is testing, the remaining ports are terminated with a 50-Ω load. The peak gains for ports 1 and 2 are 6.7 and 7.1 dBi, respectively. The far-field radiation patterns match between simulation and measurement.

The radiation pattern plots shown in Fig. 14 at scan angles of 0°, 10°, 20°, and 25° demonstrate the maximum gains of 12.9, 12.2, 10.9, and 10.3 dBi, respectively. The test results align closely with the simulation outcomes, showcasing an error margin of less than 1.5 dBi.

(b)

(b)

Fig. 13. State 1 simulated and measured element radiation patterns. (a) Port 1. (b) Port 2 (solid: simulation and dashed: measurement).
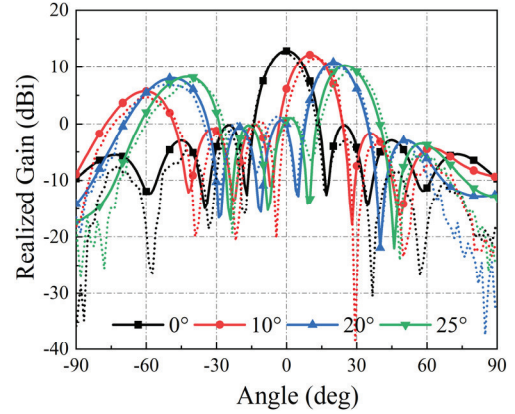
Fig. 14. State 1 simulated and measured beam-scanning radiation patterns solid: simulation and dashed: measurement).

(a)

(b)

(c)

(d)
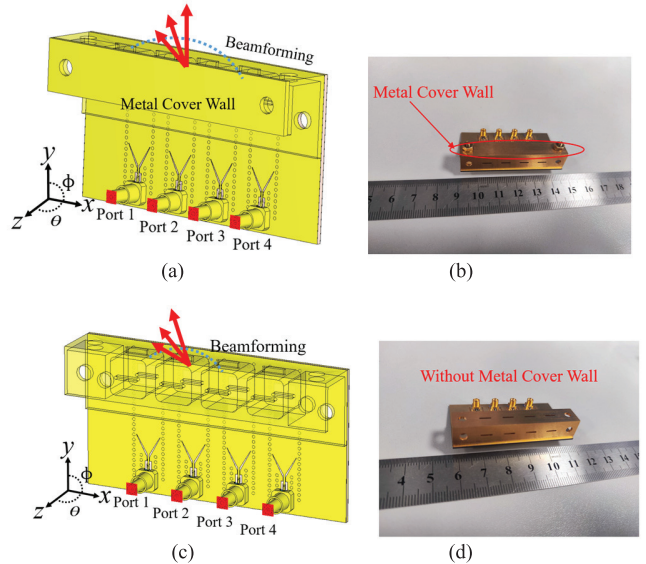
Fig. 15. States 2 and 3 geometrical configuration of the phased antenna array. (a) State 2 simulation. (b) State 2 fabrication. (c) State 3 simulation. (d) State 3 fabrication.

B. State 2

Fig. 15 represents the geometrical layout of State 2 in the phased antenna array. In Fig. 15(a), the simulated antenna structure reveals a metal cover wall obstructing the cavity slot in the $+z$-direction. Fig. 15(b) represents the manufactured antenna.
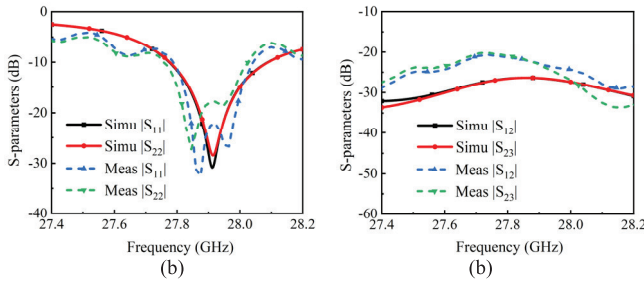
Fig. 16. State 2. (a) Simulated and measured reflection coefficients for ports 1 and 2. (b) Simulated and measured between nearby ports (solid: simulation and dashed: measurement).

Fig. 17. State 2 simulated and measured element radiation patterns. (a) Port 1. (b) Port 2 (solid: simulation and dashed: measurement).

Fig. 18. State 2 simulated and measured beam-scanning radiation patterns solid: simulation and dashed: measurement).

Fig. 19. State 3. (a) Simulated and measured reflection coefficients for ports 1 and 2. (b) Simulated and measured between nearby ports (solid: simulation and dashed: measurement).
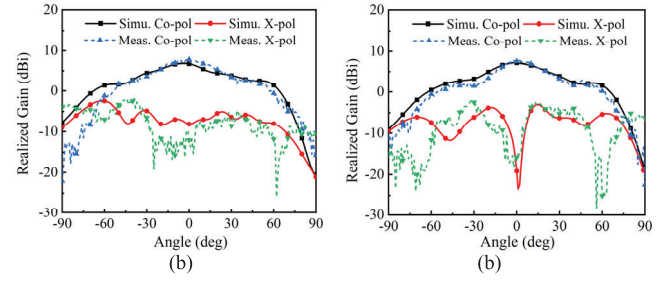

Fig. 20. State 3 simulated and measured element radiation patterns. (a) Port 1. (b) Port 2 (solid: simulation and dashed: measurement).

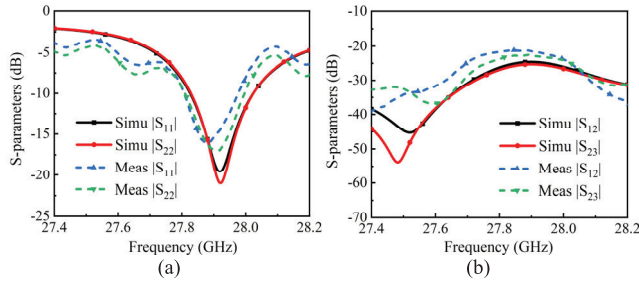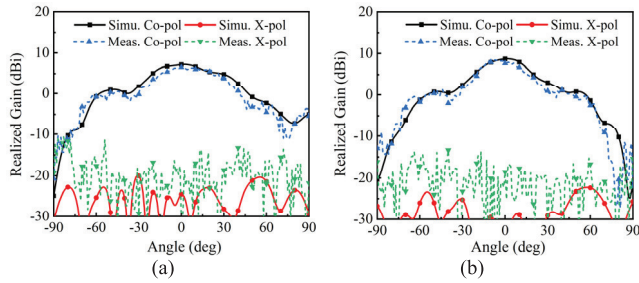Fig. 16(a) shows the reflection coefficients from both simulations and measurements. The ports are symmetrical, and at 27.91 GHz, both ports 1 and 2 exhibit return losses of less than −10 dB in simulations and measurements. Fig. 16(b) shows that both the simulated and measured return losses between adjacent ports at 27.91 GHz are below −20 dB. The measured results are in good agreement with the simulated results. Similarly, the generation of ripple in return loss is attributed to the RF cable and hand soldering parts.

Fig. 17 displays that during single-port testing, the remaining ports are connected to a 50-Ω load. The peak gains for ports 1 and 2 are 7.2 and 8.7 dBi, respectively, with cross polarization levels remaining below −10 dBi. The simulated and measured far-field radiation patterns are in good agreement, albeit slightly higher cross-polarization during testing due to the influence of test cables disturb the radiation pattern. As depicted in Fig. 18, the radiation pattern plots at scan angles of 0°, 10°, 20°, and 25° indicate the maximum gains of 14.13, 13.3, 11, and 9.84 dBi, respectively. Test results closely mirror simulation data, showing an error of less than 1 dBi. Acceptable errors include the effects of environmental scattering, welding, and machining inaccuracies.

C. State 3

The simulated antenna structure for State 3, depicted in Fig. 15(c), does not include metal cover walls in both the $+z$- and $+y$-directions. Fig. 15(d) exhibits the processed antenna structure for State 3.

Fig. 19(a) reveals that for State 3, both the simulated and measured reflection coefficients for ports 1 and 2 fall below −10 dB at 27.91 GHz. Additionally, Fig. 19(b) illustrates that the return losses between adjacent ports are below −20 dB in both the simulation and measurement results.
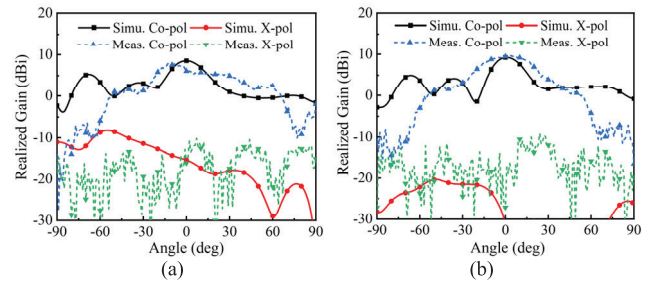
For State 3, Fig. 20 displays the simulated and measured element radiation patterns, indicating peak gains of 8.5 dBi for port 1 and 9.2 dBi for port 2. The implementation of State 3 enables the concurrent existence of two modes, TE_{101} and TM_{110}, contributing to an effective increase in antenna gain. Validation through testing indicates that both simulated and tested cross-polarization levels remain below −10 dB, affirming the viability of the proposed model. Employing the BBOX for testing beam-scanning capabilities, Fig. 21 displays the simulated and measured beam-scanning radiation patterns for State 3. Additionally, Fig. 21 illustrates radiation pattern plots at scan angles of 0°, 10°, 20°, and 25°, showing respective maximum gains of 14.9, 14.5, 13.4, and 12.4 dBi.

TABLE II
COMPARISONS WITH REPORTED RECONFIGURABLE ANTENNAS

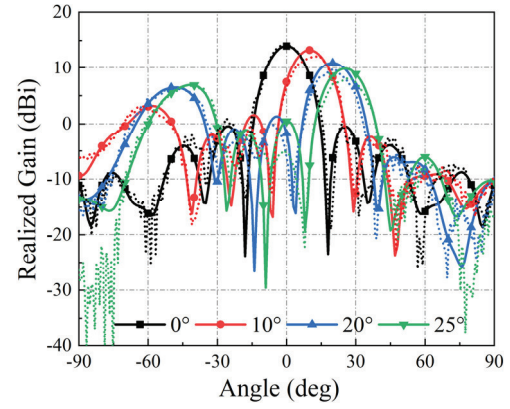| Ref.	Configuration	Control Quantity	Tuning Mechanism	Reconfiguration capability	Band	Beam direction	Power capacity
[18]	Microstrip dipole	Cell	p-i-n Diodes	Radiation pattern	Millimeter wave	End-fire/Broadside	Low
[20]	Microstrip patch	Cell	Liquid metal	Frequency/Polarization Polarization	Microwave	Broadside	Low
[21]	DRA	Cell	Dielectric Liquid	Radiation pattern Polarization	Microwave	Broadside	Low
[22]	Metal cavity	Cell	Metal screw	Frequency	Microwave	Broadside	High
[23]	Metal cavity	Array	Metal screw	Frequency/ Polarization	Microwave	Broadside	High
[24]	Cavity-backed	Cell	Tunable Slot	Frequency	Microwave	Broadside	High
[27]	Fabry–Pérot Cavity	Array	Mechanically rotated	Frequency	Millimeter wave	Broadside	Low
[28]	Cavity-backed	Array	Mechanically rotated	Polarization	Millimeter wave	Broadside	Low
[29]	Vivaldi	Cell	Graphene	Radiation pattern	Millimeter wave	End-fire	Low
This work	Metal cavity	Array	Metal cover wall	Radiation pattern	Millimeter wave	End-fire/Oblique/Broadside	High

Fig. 21.   State 3 simulated and measured beam-scanning radiation patterns solid: simulation and dashed: measurement).

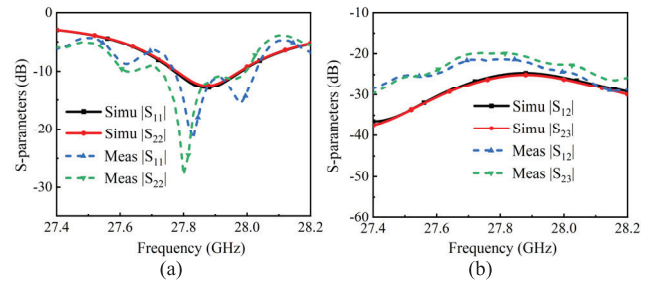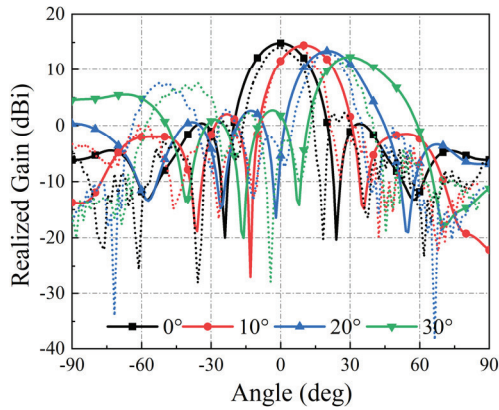Due to its symmetrical structure, only one side of the beam-scanning range is depicted.

IV. DISCUSSION

A. Stable Millimeter-Wave Array Control

In the millimeter-wave domain, the available mechanical reconfigurable methods are relatively limited. As shown in Table II, most reported reconfigurable antennas use mechanically rotating arrays or reflective arrays to adjust beam direction, which provides limited reconfigurability. Currently, no technology employs metal cover walls for antenna reconfiguration. With the higher manufacturing demands of 5G and 6G, traditional mechanical reconfiguration methods struggle to function effectively at millimeter-wave frequencies. However, metal cover walls overcome impedance mismatches and radiation instability from insufficient manufacturing precision in millimeter-wave devices, enabling the entire array's reconfigurability with fewer drive motors—an essential advancement for future 5G and 6G communications. It should be noted that this method is specifically developed for linear arrays and does not directly apply to 2-D array structures.

B. Full-Metal Structure

The full-metal antenna structure supports high-power applications, which is essential for future 5G and 6G wireless communications. Reconfigurable technology enables functional multiplexing in full-metal antennas, mitigating the disadvantage of larger volume. To validate the concept and conduct phased array tests, integrated SIW feeding is used. Notably, for high-power applications, the feeding method can be replaced by a full-metal waveguide instead of SIW.

C. Combining Phased Array and Mechanical Control

Several researchers have explored polarization, frequency, and single-direction beam reconfiguration. However, future communications, such as 5G and 6G, demand broader beam coverage, and achieving wide-angle pattern reconfiguration to cover broadside, oblique, and endfire radiation remains unresolved. This design aims to enable radiation in multiple directions by tuning different states, integrating mechanical and phase reconfiguration for extensive spatial beam coverage. This is crucial for the practical implementation of millimeter-wave technology.

V. CONCLUSION

Within this article, a novel approach for reconfiguring the millimeter-wave spectrum using metal cover walls is introduced for the first time in the existing literature. This innovative method forms the basis for the design of a reconfigurable cavity antenna capable of multiple-mode resonance. The proposed structure achieves three distinct beam forms, e.g., broadside, oblique, and endfire, by tuning different states at the same frequency. The TE_{101} mode covers endfire radiation, the TM_{110} mode covers broadside radiation, and both the TE_{101} and TM_{110} modes simultaneously excited encompass oblique radiation. Employing this methodology, a 1×4 reconfigurable phased array antenna operating in the millimeter-wave spectrum is devised. Moreover, this proposed reconfigurable antenna array achieves a beam-scanning range

of 50°, yielding a gain greater than 9 dBi. By combining phased array with three-state mechanical reconfigurability, this design is anticipated to play a crucial role in future communication systems, including 5G and 6G base stations.

REFERENCES

[1] L. Ge, M. Li, Y. Li, H. Wong, and K.-M. Luk, "Linearly polarized and circularly polarized wideband dipole antennas with reconfigurable beam direction," *IEEE Trans. Antennas Propag.*, vol. 66, no. 4, pp. 1747–1755, Apr. 2018.

[2] Y. Ji, L. Ge, Y. Li, and J. Wang, "Wideband polarization agile dielectric resonator antenna with reconfigurable broadside and conical beams," *IEEE Trans. Antennas Propag.*, vol. 70, no. 8, pp. 7169–7174, Aug. 2022.

[3] J. Hu, X. Yang, L. Ge, Z. Guo, Z.-C. Hao, and H. Wong, "A reconfigurable 1×4 circularly polarized patch array antenna with frequency, radiation pattern, and polarization agility," *IEEE Trans. Antennas Propag.*, vol. 69, no. 8, pp. 5124–5129, Aug. 2021.

[4] J. Yang, J. Li, S. Zhou, D. Li, and G. Yang, "A polarization and frequency reconfigurable microstrip antenna for vehicular communication system application," *IEEE Trans. Veh. Technol.*, vol. 72, no. 1, pp. 623–631, Jan. 2023.

[5] S.-T. Wang and L. Zhu, "Proposal and design of a null reconfigurable patch antenna on the basis of multimode method," *IEEE Trans. Antennas Propag.*, vol. 71, no. 8, pp. 6286–6296, Aug. 2023.

[6] G. Kong, X. Li, Q. Wang, and J. Zhang, "A wideband reconfigurable dual-branch helical reflectarray antenna for high-power microwave applications," *IEEE Trans. Antennas Propag.*, vol. 69, no. 2, pp. 825–833, Feb. 2021.

[7] J. Choi et al., "Frequency-adjustable planar folded slot antenna using fully integrated multithrow function for 5G mobile devices at millimeter-wave spectrum," *IEEE Trans. Microw. Theory Techn.*, vol. 68, no. 5, pp. 1872–1881, May 2020.

[8] J. Rao, Y. Zhang, S. Tang, Z. Li, C.-Y. Chiu, and R. Murch, "An active reconfigurable intelligent surface utilizing phase-reconfigurable reflection amplifiers," *IEEE Trans. Microw. Theory Tech.*, vol. 71, no. 7, pp. 3189–3202, Jul. 2023.

[9] T. Guo, W. Leng, A. Wang, J. Li, and Q. Zhang, "A novel planar parasitic array antenna with frequency- and pattern-reconfigurable characteristics," *IEEE Antennas Wireless Propag. Lett.*, vol. 13, pp. 1569–1572, 2014.

[10] L. Ge and K.-M. Luk, "A band-reconfigurable antenna based on directed dipole," *IEEE Trans. Antennas Propag.*, vol. 62, no. 1, pp. 64–71, Jan. 2014.

[11] F. Wu and K. M. Luk, "Single-port reconfigurable magneto-electric dipole antenna with quad-polarization diversity," *IEEE Trans. Antennas Propag.*, vol. 65, no. 5, pp. 2289–2296, May 2017.

[12] Y. Qin, L. Zhang, C. Mao, and H. Zhu, "Low-profile compact tri-band multimode reconfigurable antenna using characteristic mode analysis," *IEEE Trans. Antennas Propag.*, vol. 71, no. 7, pp. 6144–6149, Jul. 2023.

[13] X. Jin, S. Liu, Y. Yang, and Y. Zhou, "A frequency-reconfigurable planar slot antenna using S-PIN diode," *IEEE Antennas Wireless Propag. Lett.*, vol. 21, no. 5, pp. 1007–1011, May 2022.

[14] P. Liu, Y. Li, and Z. Zhang, "Circularly polarized 2 bit reconfigurable beam-steering antenna array," *IEEE Trans. Antennas Propag.*, vol. 68, no. 3, pp. 2416–2421, Mar. 2020.

[15] M. Li, Z. Yang, Z. Zhang, M.-C. Tang, and L. Zhu, "Miniaturized, slow-wave transmission line-based annular ring antenna with reconfigurable circular polarization and high gain," *IEEE Antennas Wireless Propag. Lett.*, vol. 22, no. 7, pp. 1766–1770, Jul. 2023.

[16] S. Zhao, Z. Wang, and Y. Dong, "A planar pattern-reconfigurable antenna with stable radiation performance," *IEEE Antennas Wireless Propag. Lett.*, vol. 21, no. 4, pp. 784–788, Apr. 2022.

[17] Z. Ding, J. Chen, H. Zhou, and R. Jin, "Two-dimensional scanning phased array with large element spacing using pattern reconfigurable stacked patch antenna at Ka-band," *IEEE Trans. Antennas Propag.*, vol. 70, no. 7, pp. 5447–5457, Jul. 2022.

[18] J. Zhang, S. Zhang, Z. Ying, A. S. Morris, and G. F. Pedersen, "Radiation-pattern reconfigurable phased array with p-i-n diodes controlled for 5G mobile terminals," *IEEE Trans. Microw. Theory Techn.*, vol. 68, no. 3, pp. 1103–1117, Mar. 2020.

[19] X. Yang, Y. Liu, H. Lei, Y. Jia, P. Zhu, and Z. Zhou, "A radiation pattern reconfigurable Fabry–Pérot antenna based on liquid metal," *IEEE Trans. Antennas Propag.*, vol. 68, no. 11, pp. 7658–7663, Nov. 2020.

[20] V. T. Bharambe, J. Ma, M. D. Dickey, and J. J. Adams, "RESHAPE: A liquid metal-based reshapable aperture for compound frequency, pattern, and polarization reconfiguration," *IEEE Trans. Antennas Propag.*, vol. 69, no. 5, pp. 2581–2594, May 2021.

[21] J. Ren et al., "Radiation pattern and polarization reconfigurable antenna using dielectric liquid," *IEEE Trans. Antennas Propag.*, vol. 68, no. 12, pp. 8174–8179, Dec. 2020.

[22] R. S. Chen et al., "Novel reconfigurable full-metal cavity-backed slot antennas using movable metal posts," *IEEE Trans. Antennas Propag.*, vol. 69, no. 10, pp. 6154–6164, Oct. 2021.

[23] R.-S. Chen et al., "Reconfigurable full-metal circularly-polarized cavity-backed slot antenna and array with frequency and polarization agility," *IEEE Trans. Circuits Syst. II, Exp. Briefs*, vol. 70, no. 2, pp. 531–535, Feb. 2023.

[24] A. Semnani, M. D. Sinanis, and D. Peroulis, "An evanescent-mode cavity-backed high-power tunable slot antenna," *IEEE Trans. Antennas Propag.*, vol. 67, no. 6, pp. 3712–3719, Jun. 2019.

[25] H. S. Lin, L. W. Mou, and Y. J. Cheng, "High-efficiencywide-angle scanning mechanoelectrical hybrid phased array antenna with mechanically reconfigurable element pattern," *IEEE Antennas Wireless Propag. Lett.*, vol. 22, pp. 1567–1571, 2023.

[26] X. Wu, Z. Li, Z. Zhang, X. Wang, L. Si, and W. Zhu, "Mechanically reconfigurable folded reflectarray antenna for variable near-field focusing," *IEEE Trans. Antennas Propag.*, vol. 71, no. 12, pp. 10038–10043, Dec. 2023.

[27] M. Li et al., "A millimeter-wave frequency-reconfigurable Fabry–Pérot cavity antenna," *IEEE Antennas Wireless Propag. Lett.*, vol. 21, pp. 1537–1541, 2022.

[28] S.-L. Chen, Y. Liu, H. Zhu, D. Chen, and Y. J. Guo, "Millimeter-wave cavity-backed multi-linear polarization reconfigurable antenna," *IEEE Trans. Antennas Propag.*, vol. 70, no. 4, pp. 2531–2542, Apr. 2022.

[29] C. Fan, B. Wu, Y. Hu, Y. Zhao, and T. Su, "Millimeter-wave pattern reconfigurable Vivaldi antenna using tunable resistor based on graphene," *IEEE Trans. Antennas Propag.*, vol. 68, no. 6, pp. 4939–4943, Jun. 2020.

[30] N. Ojaroudiparchin, M. Shen, S. Zhang, and G. F. Pedersen, "A switchable 3D-coverage-phased array antenna package for 5G mobile terminals," *IEEE Antennas Wireless Propag. Lett.*, vol. 15, pp. 1747–1750, 2016.

[31] W.-W. Yang, X.-H. Ding, T.-W. Chen, L. Guo, W. Qin, and J.-X. Chen, "A shared-aperture antenna for (3.5, 28) GHz terminals with end-fire and broadside steerable beams in millimeter wave band," *IEEE Trans. Antennas Propag.*, vol. 70, no. 10, pp. 9101–9111, Oct. 2022.

[32] D. Manteuffel, F. H. Lin, T. Li, N. Peitzmeier, and Z. N. Chen, "Characteristic mode-inspired advanced multiple antennas: Intuitive insight into element-, interelement-, and array levels of compact large arrays and metantennas," *IEEE Antennas Propag. Mag.*, vol. 64, no. 2, pp. 49–57, Apr. 2022.

[33] Z. Zhang, S.-W. Wong, R. Chen, S.-Q. Zhang, G. Huang, and Y. He, "A triple-band triple-polarization endfire/broadside millimeter-wave phased array cavity antenna with small frequency ratio," *IEEE Antennas Wireless Propag. Lett.*, vol. 23, no. 11, pp. 3461–3465, Nov. 2024.

[34] N. Peitzmeier and D. Manteuffel, "Upper bounds and design guidelines for realizing uncorrelated ports on multimode antennas based on symmetry analysis of characteristic modes," *IEEE Trans. Antennas Propag.*, vol. 67, no. 6, pp. 3902–3914, Jun. 2019.

[35] Z. Zhang, S.-W. Wong, Y. Wen, S.-Q. Zhang, W. Li, and Y. He, "A full-metal dual-band millimeter-wave antenna array with concomitant multifold orthogonal beamforming for V2V and V2I communications," *IEEE Trans. Veh. Technol.*, vol. 73, no. 7, pp. 10381–10389, Jul. 2024.

[36] TMYTEK. *BBox—Beamformer-in-a-Box*. Accessed: Jun. 26, 2025. [Online]. Available: https://www.tmytek.com/products/beamformers/bbox

[37] *Starlink*. Accessed: Jun. 26, 2025. [Online]. Available: https://www.starlink.com

Zhonghe Zhang (Member, IEEE) was born in Jinzhong, Shanxi, China, in 1995. He received the B.S. and M.E. degrees from North University of China, Taiyuan, China, in 2018 and 2021, respectively, and the Ph.D. degree from the College of Electronics and Information Engineering, Shenzhen University, Shenzhen, China, in 2024.

He is currently a Post-Doctoral Researcher with Shenzhen University. His current research interests include millimeter-wave antennas and arrays, reconfigurable antennas and arrays, multibeam antennas, and arrays.

Sai-Wai Wong (Senior Member, IEEE) received the B.S. degree in electronic engineering from The Hong Kong University of Science and Technology, Hong Kong, in 2003, and the M.Sc. and Ph.D. degrees in communication engineering from Nanyang Technological University, Singapore, in 2006 and 2009, respectively.

From July 2003 to July 2005, he was an Electronic Engineer to lead the Electronic Engineering Department in China with two Hong Kong manufacturing companies. From May 2009 to October 2010, he was a Research Fellow with the A*STAR Institute for Infocomm Research, Singapore. Since 2010, he has been an Associate Professor and later become a Full Professor with the School of Electronic and Information Engineering, South China University of Technology, Guangzhou, China. Since 2017, he has been a Tenured Full Professor with the College of Electronics and Information Engineering, Shenzhen University, Shenzhen, China. So far, he has authored and co-authored more than 200 papers in international journals and conference proceedings. His current research interests include RF/microwave circuit and antenna design.

Dr. Wong was a recipient of the New Century Excellent Talents in University awarded by the Ministry of Education of China in 2013 and Shenzhen Overseas High-Caliber Personnel Level C in 2018.

Jing-Yu Lin (Member, IEEE) received the B.E. degree from Southwest Jiaotong University (SWJTU), Chengdu, China, in 2016, the M.E. degree from South China University of Technology (SCUT), Guangzhou, China, in 2018, and the Ph.D. degree in University of Technology Sydney (UTS), Ultimo, NSW, Australia, 2022.

From October 2017 to February 2019, he was an Exchange Student with UTS. He is currently an Associate Professor with the School of Electronic Science and Engineering, Xiamen University, Xiamen, China. His current research interests include microwave, millimeter-wave, and terahertz circuit and antenna designs.

Dr. Lin was a recipient of the IEEE MTT-S Graduate Student Fellowship Awards in 2020, Xiamen University Nanqiang Talent Plan Class B, and the Marie Skłodowska-Curie Actions Postdoctoral Fellowship in 2022.

Jiupei Shi received the B.S. degree in electronics science and technology and the M.S. degree in radio physics from Xinyang Normal University, Xinyang, China, in 2018 and 2022, respectively. She is currently pursuing the Ph.D. degree in information and communication engineering with Shenzhen University, Shenzhen, China.

Her research interests include mmWave antennas, RF energy harvesting, and wireless power transmission.

Wenting Li (Member, IEEE) received the B.S. degree in electronic information engineering and the M.S. degree in electromagnetic field and microwave technology from Northwestern Polytechnical University, Xi'an, China, in 2011 and 2014, respectively, and the Ph.D. degree in electronic engineering from the University of Kent, Canterbury, U.K. in 2019.

He is currently an Assistant Professor with the College of Electronics and Information Engineering, Shenzhen University, Shenzhen, China. His current research interests include reflectarray antennas, reconfigurable antennas, circularly polarized antennas, and multibeam antennas.

Dr. Li is a recipient of Shenzhen Overseas High-Caliber Personnel Level C ("Peacock Plan Award" C).

Long Zhang (Member, IEEE) received the B.S. and M.S. degrees in electrical engineering from the Huazhong University of Science and Technology (HUST), Wuhan, China, in 2009 and 2012, respectively, and the Ph.D. degree in electronic engineering from the University of Kent, Canterbury, U.K., in 2017.

From January 2018 to April 2018, he was a Research Fellow with the Poly-Grames Research Center, Polytechnique Montreal, Montreal, QC, Canada. He is currently an Associate Professor with the College of Electronics and Information Engineering, Shenzhen University, Shenzhen, China. His current research interests include millimeter-wave antennas and arrays, tightly coupled arrays, reflectarrays and transmitarrays, characteristic mode theory, and machine-learning methods for antenna and metasurface design.

Dr. Zhang has served as a TPC Member and the session chair for several international conferences. He served as a Lead Guest Editor for Electronics Letters for a Special Issue on "Wideband/Multiband Millimeter-Wave Antennas for 5G/6G and Radar Applications" in 2023. He also serves as a reviewer for several technique journals.

Chaoyun Song (Senior Member, IEEE) received the B.E., M.S., and Ph.D. degrees in electrical engineering and electronics from the University of Liverpool, Liverpool, U.K., in 2012, 2013, and 2017, respectively.

He is currently a Distinguished Professor with the State Key Laboratory of Radio Frequency Heterogeneous Integration, Shenzhen University, Shenzhen, China, an Associate Professor (Senior Lecturer) with the Department of Engineering, King's College London, London, U.K. Prior to this, he was an Assistant Professor with the School of Engineering and Physical Sciences, Heriot-Watt University, Edinburgh, U.K. He has published more than 150 papers (including 59 IEEE transactions) in peer-reviewed journals and conference proceedings. His current research interests include wireless energy harvesting and power transfer, rectifying antennas (rectennas), flexible and stretchable electronics, metamaterials and meta-surface, and low-power sensors.

Dr. Song was a recipient of numerous international awards, including the Inaugural Best Paper Award of the PROCEEDING OF THE IEEE, the IEEE AP-S Young Professional Ambassador 2023, the IEEE AP-S Raj Mittra Travel Grant 2023, the EuCAP 2023 Best Antenna Paper Award, the IET Innovation Award in 2018, and the BAE Systems Chairman's Award in 2017. Additionally, he has served as the Session Chair and/or a TPC Member for various conferences, including EuCAP2018, IEEE AP-S Symposium 2021, IEEE VTC2022-Fall, EuCAP2023, IEEE AP-S Symposium 2023, and EuCAP2024. He has consistently contributed as a reviewer for esteemed journals, such as *Nature Electronics*, *Nature Communications, Advanced Materials*, *Advanced Functional Materials*, and *Nano Energy*, in addition to reviewing for over 15 IEEE TRANSACTIONS. He is a Top-200 reviewer for IEEE TRANSACTIONS ON ANTENNA AND PROPAGATION from 2021 to 2023. He has also taken on the role of Guest Editor of prestigious publications, including IEEE ANTENNAS AND WIRELESS PROPAGATION LETTERS, IEEE OPEN JOURNAL ON ANTENNAS AND PROPAGATION, and *IET Electronic Letters*.

Yejun He (Senior Member, IEEE) received the Ph.D. degree in information and communication engineering from Huazhong University of Science and Technology (HUST), Wuhan, China, in 2005.

From 2005 to 2006, he was a Research Associate with the Department of Electronic and Information Engineering, The Hong Kong Polytechnic University, Hong Kong. From 2006 to 2007, he was a Research Associate with the Department of Electronic Engineering, Faculty of Engineering, The Chinese University of Hong Kong, Hong Kong. In 2012, he joined the Department of Electrical and Computer Engineering, University of Waterloo, Waterloo, ON, Canada, as a Visiting Professor. From 2013 to 2015, he was an Advanced Visiting Scholar (Visiting Professor) with the School of Electrical and Computer Engineering, Georgia Institute of Technology, Atlanta, GA, USA. From 2023 to 2024, he is an Advanced Research Scholar (Visiting Professor) with the Department of Electrical and Computer Engineering, National University of Singapore, Singapore. Since 2006, he has been a Faculty Member with Shenzhen University, Shenzhen, China, where he is currently a Full Professor with the College of Electronics and Information Engineering, the Director of the Sino-British Antennas and Propagation Joint Laboratory of Ministry of Science and Technology of the People's Republic of China (MOST), the Director of Guangdong Engineering Research Center of Base Station Antennas and Propagation, the Director of Shenzhen Key Laboratory of Antennas and Propagation, and the Chair of the IEEE Antennas and Propagation Society-Shenzhen Chapter. He has authored or co-authored more than 330 refereed journal and conference papers and seven books. He holds over 20 patents. His research interests include wireless communications, antennas, and radio frequency.

Dr. He is a fellow of IET. He was selected as an "Expert with Special Government Allowance from the State Council in China," a Fellow of China Institute of Communications, a Leading Talent in the "Guangdong Special Support Program" in 2024, and the Shenzhen "Pengcheng Scholar" Distinguished Professor, China, in 2020, respectively. He received Shenzhen Overseas High-Caliber Personnel Level B ("Peacock Plan Award" B) and Shenzhen High-Level Professional Talent (Local Leading Talent). He received the Second Prize of Guangdong Provincial Science and Technology Progress Award in 2023, the 10th Guangdong Provincial Patent Excellence Award in 2023, the Second Prize of Shenzhen Science and Technology Progress Award in 2017, and the Three Prize of Guangdong Provincial Science and Technology Progress Award in 2018. He also obtained the 2022 IEEE APS Outstanding Chapter Award. He is the Principal Investigator for over 40 current or finished research projects, including the National Natural Science Foundation of China, the Science and Technology Program of Guangdong Province, and the Science and Technology Program of Shenzhen City. He has served as a reviewer for various journals, such as IEEE TRANSACTIONS ON VEHICULAR TECHNOLOGY, IEEE TRANSACTIONS ON COMMUNICATIONS, IEEE TRANSACTIONS ON INDUSTRIAL ELECTRONICS, IEEE TRANSACTIONS ON ANTENNAS AND PROPAGATION, IEEE WIRELESS COMMUNICATIONS, IEEE COMMUNICATIONS LETTERS, *International Journal of Communication Systems*, and *Wireless Personal Communications*. He has also served as a Technical Program Committee Member or a Session Chair for various conferences, including the IEEE Global Telecommunications Conference (GLOBECOM), the IEEE International Conference on Communications (ICC), the IEEE Wireless Communication Networking Conference (WCNC), and the IEEE Vehicular Technology Conference (VTC). He served as the TPC Chair for IEEE ComComAp 2021 and the General Chair for IEEE ComComAp 2019. He was selected as a Board Member of the IEEE Wireless and Optical Communications Conference (WOCC). He acted as the Publicity Chair of several international conferences, such as the IEEE PIMRC 2012. He served as the TPC Co-Chair for WOCC 2023/2022/2019/2015, APCAP 2023, UCMMT 2023, ACES-China2023, and NEMO 2020; and the Executive Chair for the 2024 IEEE International Workshop of Radio Frequency and Antenna Technologies (RFAT 2024). He is serving as the Executive Chair for the 2025 IEEE International Workshop of Radio Frequency and Antenna Technologies (RFAT 2025). He is serving as an Associate Editor for IEEE TRANSACTIONS ON ANTENNAS AND PROPAGATION, IEEE TRANSACTIONS ON VEHICULAR TECHNOLOGY, IEEE TRANSACTIONS ON MOBILE COMPUTING, IEEE *Antennas* and *Propagation Magazine*, IEEE ANTENNAS AND WIRELESS PROPAGATION LETTERS, *International Journal of Communication Systems, China Communications*, and *ZTE Communications*.